REGULAR PAPER

Y. Nakaie · Y. Ohta · K. Hishida

Flow measurement around a cycloidal propeller

Abstract An experimental investigation was conducted to study the flow around a cycloidal propeller. Flow fields were obtained using a particle image velocimetry system whose data acquisition was synchronized with the propeller's angular position. The chord-based Reynolds number was $Re_c = u_r c / v = 1.4 \times 10^4$, where u_r is the rotational velocity of the propeller and c is the chord length of the airfoil. Flow characteristics such as mean velocity, vorticity and the RMS value of velocity fluctuation were derived from the measurements. The results demonstrated the presence of a downwash around the propeller during the generation of lift. Detailed observations around each airfoil visualized distinct vortex shedding and reattaching flow at certain phase angles of the propeller.

Keywords Micro air vehicle · Cycloidal propeller · Particle image velocimetry · Phase-averaged measurements

1 Introduction

The desire to develop an unmanned miniature aircraft has increased over the last few decades. These vehicles, so-called "micro air vehicles (MAVs)", should be capable of operating in scenarios such as rescues in collapsed buildings or inspections in hazardous environments. Because such situations often require flight indoors or in confined areas, capabilities such as vertical takeoff/landing and hovering become essential. There are two common methods to achieve this type of flight: rotary airfoils (e.g., helicopters) and flapping airfoils (e.g., birds). In this study, a third method is investigated.

A "cycloidal propeller" (Fig. 1) is a term used for a multi-blade rotor that looks rather like a vertical axis wind turbine. The name originates with NASA researchers in the 1930s (Iosilevskii and Levy 2003). The most notable characteristic of the cycloidal propeller is its ability to produce force in any direction perpendicular to its rotation axis. Currently employed as propulsion systems in ships, a "cyclogyro" (a name describing a cycloidal-propellered aircraft) is expected to act as a high-performance MAV exhibiting the above-mentioned flight abilities.

Several studies have been conducted to investigate the aerodynamic performance of cyclogyros (Hashimoto et al. 2005; Iosilevskii and Levy 2006; Suzuki et al. 2004, 2005; Yoshitake et al. 2009; Yun and Park 2004). In recent research, Tanaka et al. (2007) developed a cyclogyro and varied its design parameters (wing length, wing number, etc.) to determine the combination that could generate the largest lift force. Their optimal model succeeded in tethered hovering and demonstrated the cycloidal propeller's potential ability for flight. However, to date, no successful free flight has been accomplished. Enhancement of the lift
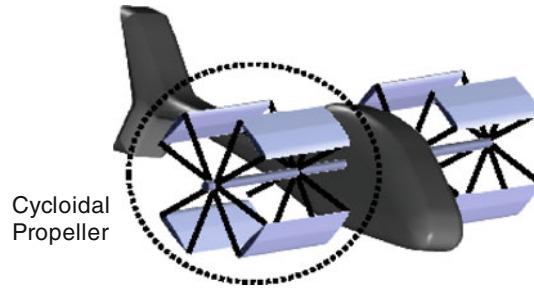
Y. Nakaie (✉) · Y. Ohta · K. Hishida
Department of System Design Engineering, Faculty of Science of Technology, Keio University, Kohoku-ku, Yokohama 223-8522, Japan
E-mail: nakaie@tfe.sd.keio.ac.jp

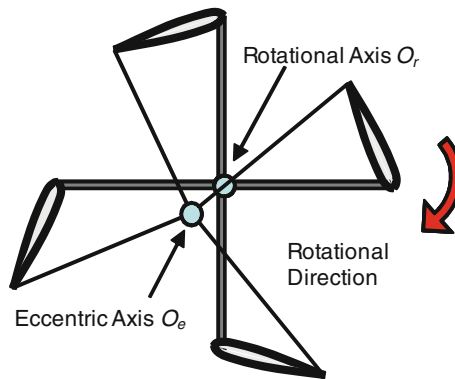**Fig. 1** Schematic illustration of a cycloidal-propellered aircraft

Fig. 2 Double crank mechanism for controlling the AOA of the airfoils

to weight (L/W) ratio still remains a challenge. To fully understand the fundamental force-generation mechanisms in cyclogyros, flow analysis around the propeller is required, which may lead to insights into improving the L/W ratio and the development of high-lift devices. The objective of this research is to obtain the detailed flow structure around the cycloidal propeller using particle image velocimetry (PIV). Phase-averaging techniques were applied to capture flow structures for different phase angles of the propeller.

2 Cycloidal propeller model

2.1 Operating principle

Cycloidal propellers produce force by changing the angle of attack (AOA) of each airfoil during its rotation. If the AOA of the airfoils is fixed at a constant value, the forces generated by the different airfoils cancel each other out, resulting in a net lift of zero.

The present study employs the variable AOA system proposed by Tanaka et al. (2007). A schematic diagram of the system is presented in Fig. 2. The leading edges of the airfoils are connected to the rotational axis O_r by shafts. The trailing edges are connected to the eccentric axis O_e, which is a distance e away from O_r. This double crank mechanism causes a periodic change in the airfoil's AOA during rotation. The maximum AOA can be modified by adjusting the eccentric distance e between the two axes. The angle of eccentricity θ_p was defined as the angle between the line connecting O_r with O_e and the y axis.

Figure 3a shows the design parameters of the cycloidal propeller model. Obviously, when $e = 0$, the AOA is fixed at a constant value. Figure 3b schematically shows a 3D view of the cycloidal propeller.

2.2 Model specifications

As summarized in Table 1, the propeller model consists of three NACA 0012 airfoils, each having with a chord length and wing span of $c = 0.045$ m and $b = 0.240$ m, respectively. The eccentric distance e was set either to 0 or 0.025 m, depending on the experimental conditions. The leading edges of the airfoils are
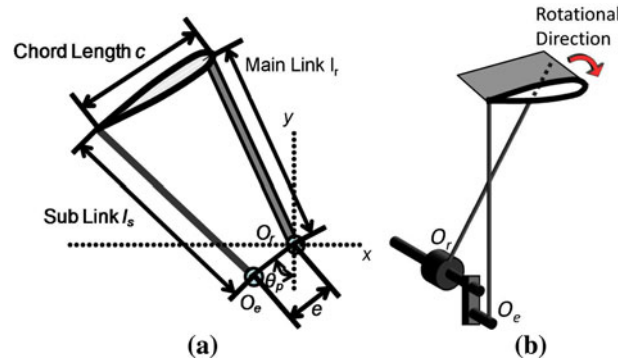
Fig. 3 **a** Design parameters of the cycloidal propeller, **b** 3D view of the cycloidal propeller

Table 1 Model specifications

Airfoil	NACA 0012
Number of airfoils n	3
Chord length c	0.045 m
Wing span b	0.240 m
Main link l_r	0.130 m
Sub link l_s	0.135 m
Eccentric distance e	0.0.025 m
Angle of eccentricity θ_p	0

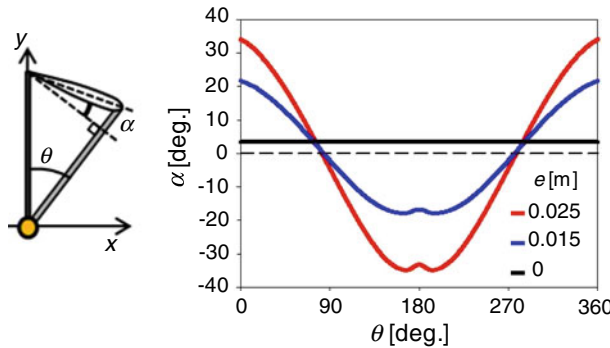**Fig. 4** Plot of AOA α against phase angle θ

connected to a stepping motor by carbon shafts. These parameters were selected to take the same values as in the optimally designed model introduced by Tanaka et al. (2007). θ_p was set to be 0°. Figure 4 shows the relationship between the propeller's phase angle θ and the airfoil's AOA α for $e = 0, 0.015$ and 0.025 m. As described previously, α varies in a periodic fashion when $e \neq 0$. In this study, the lift force is defined as the vertical force generated from whole propeller mechanism.

3 Experimental apparatus

3.1 PIV setup

Schematic of the experimental setup is shown in Figs. 5, 6. The cycloidal propeller model was placed in the test section of a $40 \times 40 \times 100$ cm^3 open circuit wind tunnel. Its rotational rate f was set at 2–6 rps, controlled by a stepping motor. The free-stream velocity was set at $U_0 = 0.5$ m/s. The Reynolds number based on the chord length of the airfoil was $Re_c = u_r c / \upsilon = 1.4 \times 10^4$ (for $f = 6$ rps). u_r is the rotational velocity of the propeller defined by $u_r = 2\pi f l_r$.
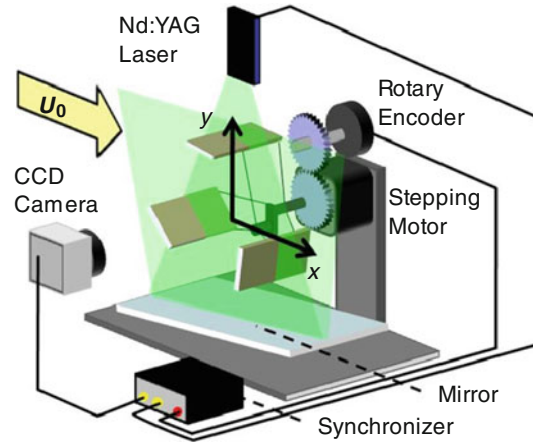
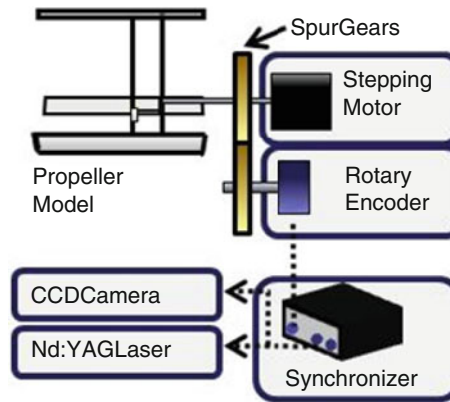**Fig. 5** Experimental setup for phase-averaged PIV

Fig. 6 Procedure for PIV data acquisition

The origin of the two-dimensional Cartesian coordinate system was located at the rotational axis O_r, with the x axis along the free-stream direction and the y axis in the vertical direction along the laser-beam sheet. The experiment was conducted with two different configurations. First, flow fields in the area $-167 \leq x \leq 180$ mm, $-268 \leq y \leq 209$ mm were measured to investigate the flow around the entire propeller. Second, measurements around each airfoil were performed in a smaller area of 146×110 mm^2.

The flow field was illuminated by a 90 mJ dual head Nd:YAG laser (New Wave Research GEMINI 30 Hz) with a wavelength of 532 nm. To illuminate the shadow regions formed beneath the airfoils, a mirror was placed below the propeller to reflect the laser sheet. The visualized flow was captured by a 12-bit CCD camera (Imperx 2 M-30-LM) with a resolution of $1,600 \times 1,200$ pixels. 120 PIV image pairs were recorded. Measurements were carried out when the phase angle of the propeller had specific values $\theta_m = 0°$, $30°$, $60°$ and $90°$ (θ_m angle of measurement). The mean velocity (U_{ave}, V_{ave}) and the RMS values of velocity fluctuations (U_{RMS}, V_{RMS}) were obtained from 480 instantaneous velocity fields (120 image pairs $\times$ 4 measurement angles). Here, U denotes velocity components along the x axis and V denotes those along the y axis.

3.2 Timing and control for phase-averaged measurements

Timing and control of the PIV system was accomplished by utilizing a rotary encoder, a pulse counter and a synchronizer. A rotary encoder is a device that converts the angular position of a rotational axis to a digital signal. In this research, a rotary encoder (NEMICON HES-036-2M) with a resolution of 360 pulse/rev was allowed to rotate synchronously with the stepping motor. During rotation, the output signals from the rotary encoder were used to measure the phase angle and also acted as external triggers for the synchronizer, which
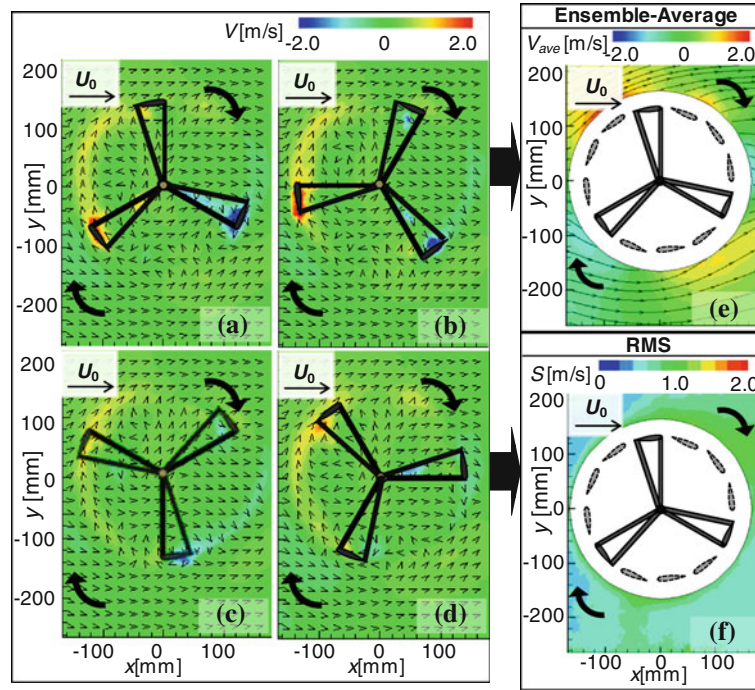
Fig. 7 Flow characteristics for $e = 0$ (constant AOA). Profiles of y-component velocity V for (**a**) $\theta_m = 0°$, (**b**) $\theta_m = 30°$, (**c**) $\theta_m = 60°$ and (**d**) $\theta_m = 90°$: profiles of **e** mean velocity V_{ave} and **f** RMS of velocity fluctuations S, derived from **a** to **d**

then sent trigger signals to the Nd:YAG laser and the CCD camera and such a system allows PIV data to be acquired at an arbitrary phase angle θ.

4 Results and discussion

4.1 Flow comparison between constant and variable AOA

The flow characteristics for a constant ($e = 0$) and a variable ($e = 0.025$) AOA are shown in Figs. 7 and 8, respectively. The curved arrows in the figures indicate the rotational direction of the cycloidal propeller. In both figures, the distribution of the y-component velocity V for $\theta_m = 0°$, 30°, 60° and 90° are seen in a–d, respectively. The profiles of the ensemble averaged velocity V_{ave} obtained from these flow fields are shown in e. The profiles of the RMS velocity fluctuation S, which is defined by

$$S = \sqrt{U_{RMS}^2 + V_{RMS}^2}$$

are presented in (F). U_{RMS} and V_{RMS} are the RMS values of the velocity fluctuation for U and V, respectively.

When comparing the two cases, when the AOA of the airfoils was constant, the velocity vectors outside the propeller indicate flow from left to right (in the same direction as the free stream), as if to avoid entering the propeller. The values of S outside the propeller do not exceed 1.5 m/s. On the other hand, a downward flow is observed around the propeller in the variable AOA case, which is in good agreement with previously published aerodynamic theory (Yun and Park 2004) and numerical results (Iosilevskii and Levy 2006; Yun and Park 2004). In addition, an area with large velocity fluctuations ($S \geq 2.0$) exists beneath the propeller. It can be said that variation in the AOA affects the unsteadiness of the flow in that region. We discussed this unsteadiness of the flow in Sect. 4.4. The fact that thrust is generated only when α is variable suggests that the downward flow is closely related to the generation of lift. In fact, it is well known that helicopter blades produce lift by forcing air to flow downward, and the reaction force pushes the propeller upwards. It is considered that a similar phenomenon was captured around the cycloidal propeller.
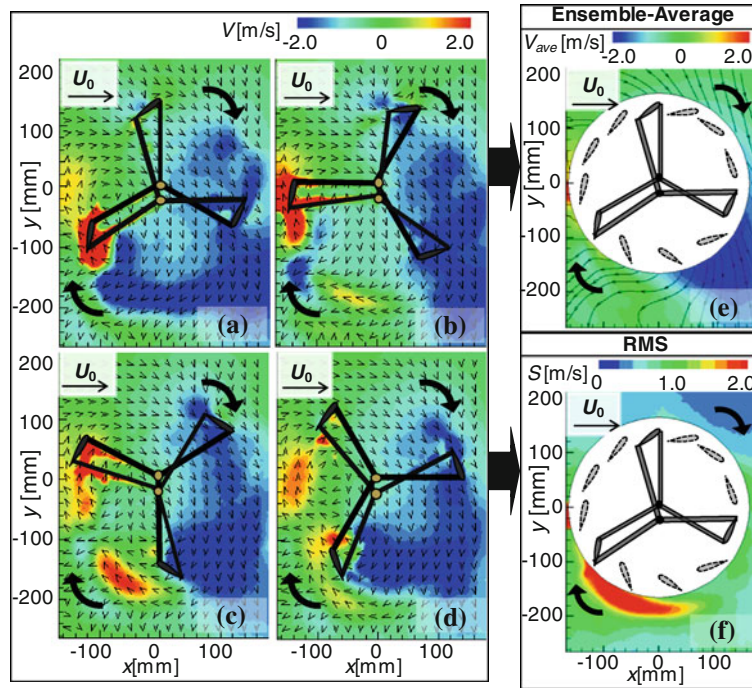
Fig. 8 Flow characteristics at $e = 0.025$ (variable AOA). Profiles of y-component velocity V for (**a**) $\theta_m = 0°$, (**b**) $\theta_m = 30°$, (**c**) $\theta_m = 60°$ and (**d**) $\theta_m = 90°$. Profiles of **e** mean velocity V_{ave} and **f** RMS of velocity fluctuations S, derived from **a** to **d**

4.2 Flow structures at different phase angles

In this section, all observed flow fields correspond to the case of variable AOA. As seen in Fig. 8, for all phase angles, the velocity fields indicate a downward flow around the propeller during the generation of lift force. In the region above the propeller, the velocity vectors are directed downward indicating flow into the rotor from the upper half of the propeller. The vectors inside the propeller are also pointing downward, in particular for $x \geq 0$.

The flow fields beneath the propeller exhibit different behavior at each phase angle. For instance, flow in the region of $-100 \leq x \leq 0$ mm, $-200 \leq y \leq -100$ mm is accelerated downward when $\theta_m = 0°$, but upward when $\theta_m = 60°$. As a result, this region contains areas with large velocity fluctuations as compared to the upper region, as is clearly seen in Fig. 8f.

4.3 Comparison of rotational frequency

The profiles of V_{ave} at $y = 160$ and -160 mm (just above and below the propeller) for a rotational frequency of 2, 4 and 6 rps are shown in Fig. 9. The phenomenon in which the main stream is diverted into and accelerated out of the propeller is clearly observed. Because more force is produced at higher frequencies, it could easily be imagined that this downwash also tends to get stronger. However, it is of note that in the profile below the propeller, the rotational frequency does not have much effect on the flow in the left-side region (highlighted in blue).

4.4 Flow structures around the airfoil

To form a more comprehensive understanding of the phenomenon occurring around the airfoil, the motion of the fluid relative to the airfoils is examined in more detail for the variable AOA case. Figures 10a and b display profiles for the magnitude of relative velocity (U_{rel}, V_{rel}) for $\theta_m = 0$ and $60°$, respectively. U_{rel} and V_{rel} were derived from the following equations:

$$U_{rel} = U - u_r \cos \theta, \quad V_{rel} = V - u_r \sin \theta$$

The lines in Fig. 10 show the streamlines around the airfoil obtained from the phase-averaged velocity distributions. Distributions of vorticity Ω for $\theta_m = 0°$ and 60 are depicted in Fig. 11. In Fig. 11a, for
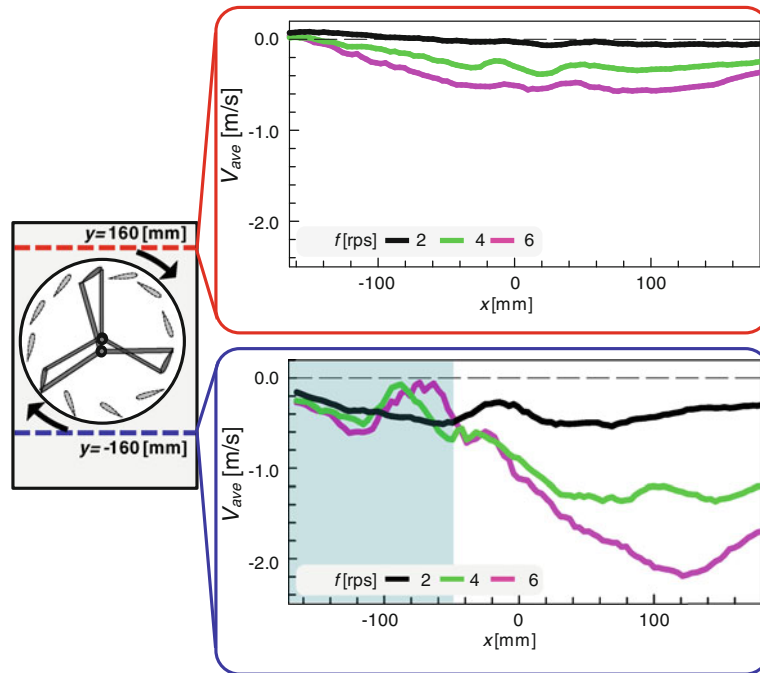
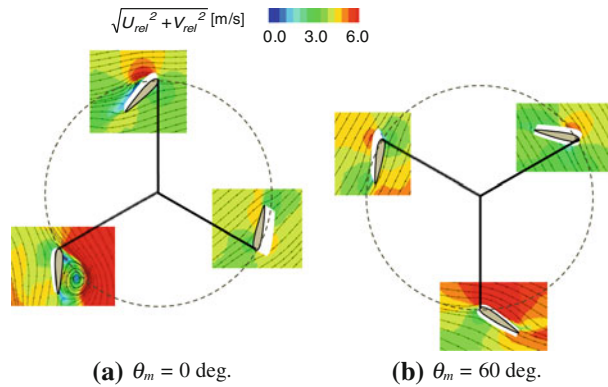**Fig. 9** Comparison of average velocity profiles above and below the propeller

(a) $\theta_m = 0$ deg.   **(b)** $\theta_m = 60$ deg.

Fig. 10 Distributions of the magnitude of relative velocity to the airfoil

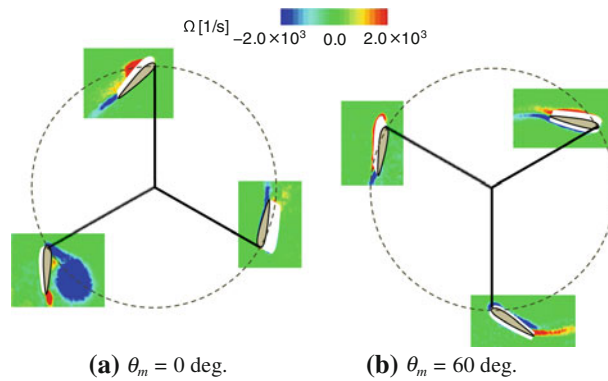**(a)** $\theta_m = 0$ deg.   **(b)** $\theta_m = 60$ deg.

Fig. 11 Distributions of vorticity relative to the airfoil

$\theta = 0°$, a recirculation zone is formed and the boundary layer reattaches to the surface of the airfoil. In addition, distinct vortex shedding from the leading edge could be confirmed at $\theta = 240°$, which indicates the possibility of dynamic stall. This phenomenon is considered to occur due to the airfoil's rotation being in the opposite direction to the downwash produced inside the propeller. According to the theory introduced by Iosilevskii and Levy (2003), the lift force generated by each airfoil reaches a maximum value around $\theta = 180°$. At this angle, the stream lines are aligned with the airfoil and no separating flow is observed. In conclusion, it was seen that the flow around each airfoil includes complex phenomena such as dynamic stall and reattaching flows.

5 Conclusion

A quantitative investigation of the flow around a cycloidal propeller was conducted using phase-averaged PIV. A phase-averaging technique utilizing a rotary encoder was employed, which enabled flow fields to be captured at any phase angle of the propeller. Experiments were performed in a wind tunnel at $Re_c = 1.4 \times 10^4$. The important conclusions are summarized below:

- A downward flow was observed when the AOA of the airfoils was variable and such flow did not occur for constant AOA.
- In the variable AOA case, the RMS profile of velocity fluctuations showed larger values in the region beneath the propeller than the region above.
- Flow characteristics relative to the airfoil revealed phenomena such as reattaching flow and vortex shedding at certain phase angles.

It is expected that the precise force generating mechanisms would be elucidated by further investigating the flow at other phase angles of the propeller together with force measurements.

References

Iosilevskii G, Levy Y (2003) Aerodynamics of the cyclogiro. In: 33rd AIAA fluid dynamics conference and exhibit, Orlando, Florida AIAA2003-3473:1–9
Iosilevskii G, Levy Y (2006) Experimental and numerical study of cyclogiro aerodynamics. AIAA J 44–12:2866–2870
Suzuki R, Tanaka K, Emaru T (2004) A flying robot with variable attack angle mechanism. ROBOMEC 2P2-L2-2
Suzuki R, Tanaka K, Emaru T (2005) Experimental study on optimal parameters of a flying robot with variable attack angle mechanism. Proc JSME Conf Robot Mechatron 2P-1-S-060
Tanaka K, Suzuki R, Emaru T, Higashi Y, Wang HO (2007) Development of a cyclogyro-based flying robot with variable attack angle mechanisms. IEEE/ASME Trans Mechatron 12–5:565–570
Yoshitake K, Shouji H, Matsuuchi K (2009) Analysis of the characteristics of cycloidal propeller with the unsteady airfoil theory. Turbomachinery 37–2:14–20
Yun CY, Park I (2004) A new VTOL UAV cyclocopter with cycloidal blades system. American Helicopter Society 60th Annual Forum, Baltimore